OPTICA

Magnetically twisted photoacoustic phase relaxation tomography for deep-tissue spatiotemporal quantitative viscography

Xiaoye Su,[1,2,†] Zhenhui Zhang,[1,2,†] Xiaokai Wang,[1,2] Piao Zhang,[1,2] Hao Li,[1,2] Shuqiqin Shi,[1,2] Dong Liu,[3] Jian Zhang,[3] Yujiao Shi,[1,2,4] and Sihua Yang[1,2,5]

[1]MOE Key Laboratory of Laser Life Science & Institute of Laser Life Science, South China Normal University, Guangzhou 510631, China
[2]Guangdong Provincial Key Laboratory of Laser Life Science, College of Biophotonics, School of Optoelectronic Science and Engineering, South China Normal University, Guangzhou 510631, China
[3]School of Biomedical Engineering, Guangzhou Medical University, Guangzhou, China
[4]shiyuj@scnu.edu.cn
[5]yangsh@scnu.edu.cn
[†]These authors contributed equally to this work.

Received 16 April 2026; revised 5 August 2026; accepted 7 August 2026; published 3 September 2026

Viscosity is a crucial biomechanical factor in energy dissipation, mass transport, and non-equilibrium dynamics in living systems. Yet, quantifying local viscosity within deep, optically opaque tissues remains a formidable challenge due to strong light scattering. Here, we present the magnetically-twisted photoacoustic phase relaxation technique revealing the spatiotemporal heterogeneity of viscosity in deep tissue by introducing magnetoplasma Fe_3O_4/Au nanorotors. The viscosity-induced phase relaxation is extracted from the phase shift between the external magnetic field and the polarization-modulated photoacoustic readout. The depth-resolved, high-fidelity viscous mechanical information is converted into rotation-modulated ultrasound signals that are capable of propagating through strongly scattering tissues. Theoretically, we establish a quantitative relationship linking viscosity to the phase relaxation based on the overdamped angular momentum balance equation of the rotor and achieve a viscosity measurement uncertainty of up to 0.17 cp at a signal-to-noise ratio of 15 dB. Experimentally, we successfully capture the dynamic viscosity evolution during blood coagulation at a 2.4 mm tissue depth and map localized viscosity profiles during early zebrafish embryogenesis. This work provides a technical foundation for visualizing viscosity as an active physical field involved in morphogenesis and dynamical regulation in living systems.

https://doi.org/10.1364/OPTICA.603085

1. INTRODUCTION

Viscosity, the physical quantity describing a fluid's resistance to flow, governs energy dissipation and transport across material systems ranging from synthetic soft matter to living organisms [1–4]. While the classical Newtonian framework treats viscosity as a homogeneous and constant parameter defining the stress–strain rate relation, real mediums often deviate from this idealization. In soft and biological matter, viscosity constitutes a spatiotemporally heterogeneous field, $\eta(r, t)$ [5–7], reflecting dynamic microstructural organization and serving as a key determinant of material behavior and function. Spatial viscosity gradients drive nonequilibrium transport and structural evolution, whereas temporal variations dictate kinetic pathways, energy dissipation modes, and the relaxation toward steady states [8–11]. In living systems, such heterogeneity directly underpins physiological processes, including viscosity patterns regulate organelle positioning, mediate force transduction within the extracellular matrix, and guide cell migration and morphogenesis during development [12–16]. During blood coagulation, the fibrinogen-to-fibrin transition induces a pronounced local viscosity increase that mirrors platelet and thrombin activity [17,18]. Consequently, resolving the spatiotemporal viscosity field is essential for elucidating the nonequilibrium physics of soft and living matter and for uncovering the biomechanical basis of physiological regulation and disease.

Despite its importance, direct measurement of spatiotemporally varying viscosity remains a major challenge. This difficulty stems from a fundamental observational mismatch: local viscous responses are defined at microscopic statistical scales, whereas most deep-imaging modalities operate through wave propagation in scattering media [19]. Wave-based viscometry, including magnetic resonance and ultrasonic shear-wave methods, infers viscosity from attenuation or dispersion of propagating modes [20–22]. Because these observables are governed by intrinsically non-local operators, the measured signal reflects dissipation integrated along the propagation path, precluding voxel-wise recovery of $\eta(r, t)$ [23,24].

Particle-tracking microrheology, by contrast, estimates viscosity from probe trajectories fitted to viscous-drag models [25–27]. Although local in principle, this requires temporal differentiation and statistical averaging over trajectories, making it sensitive to noise and unreliable in heterogeneous or dynamically evolving environments where probe motion no longer reflects purely local viscous resistance. Other techniques such as rheometry, AFM indentation, Brillouin microscopy, and photoacoustic (PA) viscoelastic imaging provide valuable mechanical information but remain limited by *ex vivo* measurement, surface confinement, or weak inelastic scattering, and therefore cannot access rapidly evolving viscosity fields deep inside living tissue [28–33]. Consequently, what is needed is not merely a more sensitive probe, but a physical observable that is both local and inherently causal, enables depth-resolved measurement of local effective viscosity and demonstrates its potential for investigating viscosity spatial mapping in scattering biological tissues.

Here, we introduce magnetically-twisted photoacoustic viscography (MTPAV), in which the viscosity-defined phase relaxation $\Delta\varphi$ serves as such a local observable for deep-tissue spatiotemporal viscography (Fig. 1). When a rotating magnetic field exerts precisely controllable periodic torsional stress on magnetic plasmonic nanorotors in a fluid, owing to viscous resistance of the fluid, the rotor rotation exhibits a phase relaxation strictly limited by the medium viscosity. Thus, the overdamped angular momentum balance equation for anisotropic rotor establishes a dynamic equilibrium between the external torque and viscous drag. Under synchronous rotation, the sine of the phase relaxation angle of the rotor is shown to be proportional to the local viscosity. As a result, $\Delta\varphi$ serves as a quantitative readout of local viscous resistance, without spatial deconvolution, temporal differentiation, or statistical inversion. Subsequently, depth-resolved polarization-resolved PA technology employs the optical anisotropy of nanorotors, where their absorption cross-section varies periodically with the angle between the particle's long axis and the polarization direction of the excitation light during rotation. By detecting the phase relaxation between the rotating magnetic field and the modulated PA signal, we achieve voxel-resolved, spatiotemporal mapping of viscosity in heterogeneous and dynamically evolving media. This capability is demonstrated by visualizing the rapid progression of viscosity during blood coagulation at a depth of 2.4 mm in thick tissue, and by obtaining the first viscosity maps of early zebrafish embryogenesis, revealing the timing and spatial organization of morphogenetic processes. This work establishes a new imaging method for viscosity as a dynamic physical field, enabling quantitative investigation of viscous mechanical behavior in living systems.

2. PRINCIPLES OF MTPAV

When a rotating magnetic field with angular frequency ω and initial phase φ_0 applies precisely controllable periodic torsional stresses to the anisotropic magnetoplasma rotor with aspect ratio L/D in a medium with viscosity η, the magnetization direction of the magnetic plasma remains quasi-statically aligned with the applied magnetic field. The rotor experiences energy dissipation due to viscous drag, resulting in a stable phase relaxation relative to the driving field's direction. Under the overdamped approximation (low Reynolds number, negligible inertial effects), the rotor's angular momentum balance equation is expressed as [34–36]

$$\gamma \frac{d\varphi}{dt} = mB\sin(\omega t + \varphi_0 - \varphi), \tag{1}$$

where γ is the viscous friction coefficient proportional to the medium viscosity η, m is the effective magnetic moment of the rotor, B is the magnetics induction strength, and φ is the rotor orientation angle. Under steady state conditions, the rotor rotates synchronously with the external field, so that $\varphi(t) = \omega t + \varphi_0 - \Delta\varphi$ substituting into Eq. (1) yields $\gamma\omega = mB\sin\Delta\varphi$. Because $\gamma \propto \eta$, the viscosity and phase relaxation are satisfied

$$\eta = C \cdot \sin\Delta\varphi, \tag{2}$$

where $C = \frac{MB}{4\omega} \cdot g(\frac{L}{D}) \cdot (\frac{L}{D})^{-2}$ is a constant related to the rotor geometry and magnetic field parameters. Equation (2) makes it clear that viscosity is directly proportional to the sine function of the phase relaxation, where L is the length of the magnetic nanorotor; D is the diameter of the nanorotor, the geometric factor $g(L/D)$ accounts for the shape-dependent hydrodynamic resistance of the nanorotor in a viscous medium. M represents the

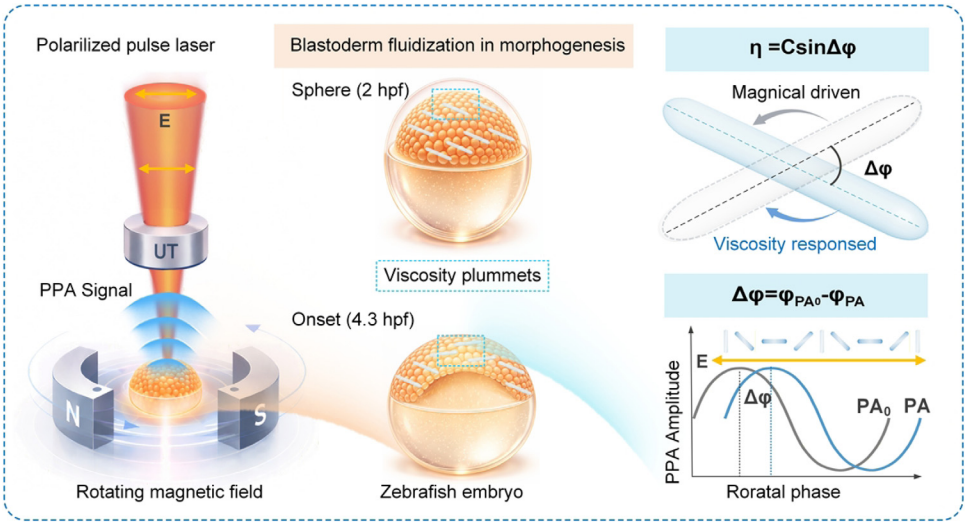

Fig. 1. Schematic of the magnetically-twisted phase-relaxation PA spatiotemporal viscography platform. A rotating magnetic field drives a magnetoplasmonic nanorotor, generating a phase-relaxation response governed by the viscous torque of the surrounding.

magnetization intensity of the particle, B represents the magnetic induction intensity of the magnetic field, and ω represents the rotational angular frequency of the magnetic field. Therefore, quantitative access to the viscosity of the medium can be realized by measuring the phase relaxation $\Delta\varphi$.

The viscosity indicator used in this experiment is custom-designed and composed of a magnetic rotor Fe_3O_4 and a polarization PA sensitive Au nanorods arranged side by side. Benefiting from the unique anisotropic optical absorption of the Au nanorods, the orientation change of rotors can be observed through PA detection, where the principal axis dictates the intensity of polarized light absorption at a fixed polarization angle. The absorption coefficient reaches its peak when the electric vector orientation of the excitation laser aligns with the principal axis φ of the rotor and reaches the minimum when perpendicular. By denoting the polarization angle of the excitation laser as ϕ, the angle between the electric vector orientation and the principal axis of the rotor is $\theta = \phi - \varphi$. The absorption coefficient can be expressed as [37,38]

$$\mu(\phi, \varphi) = \mu_0 \left(1 + \kappa \cos 2\theta\right), \tag{3}$$

where $\mu_0 = (\mu_\parallel + \mu_\perp)/2$ is the average absorption coefficient, anisotropic absorption ratio is $\kappa = \frac{\mu_\parallel - \mu_\perp}{\mu_\parallel + \mu_\perp}$, $\mu_\parallel$ and $\mu_\perp$ is the absorption coefficient of the rotor when $\theta = 0°$ and $\theta = 90°$. Therefore, when the rotor orientation rotates with the magnetic field at an angular velocity, its absorption coefficient changes periodically, which modulates the generated PA signals. According to the PA theory, the resulting PA signal amplitude can be expressed as

$$PA(t) = P_0[1 + \kappa \cos(2(\omega t + \varphi_0 - \phi - \Delta\varphi))], \tag{4}$$

where $P_0 = I_0 \cdot e^{-\alpha z} \cdot \Gamma \cdot \eta_{th} \cdot \mu_0$ is the average signal amplitude during the rotation period, $PA(t)$ denotes the rotationally modulated polarization-sensitive PA amplitude of the rotor. I_0 is the light intensity of the linearly polarized laser, and $e^{-\alpha z}$ accounts for the light attenuation with imaging depth z. Γ is the Grueneisen parameter, and η_{th} is the heat conversion efficiency.

Therefore, with the rotation of the magnetic field, the obtained PA signal amplitude changes as a cosine function. Then, the amplitude curve undergoes a fast Fourier transform (FFT) to obtain its spectral information. By extracting the modulated signal at frequency 2ω and calculating the argument (the arg operation, which represents the phase angle of the complex value) of the complex component X[2ω], the azimuth angle of rotor rotation φ can be determined as follows:

$$\varphi_{PA} = \arg(X_{PA}\,[2\omega]) = 2(\varphi_0 - \Delta\varphi - \phi). \tag{5}$$

To obtain the phase relaxation angle, system calibration is required, which involves measuring using a zero-relaxation standard calibration sample to obtain the calibrated phase:

$$\varphi_{PA_0} = \arg(X_{PA_0}\,[2\omega]) = 2(\varphi_0 - \phi). \tag{6}$$

Thus, the phase relaxation can be obtained as $\Delta\varphi = (\varphi_{PA0} - \varphi_{PA})/2$. Substituting it into the steady-state viscosity Eq. (2) yields, the viscosity can be expressed as

$$\eta = C \sin\left[\frac{1}{2}\left(\varphi_{PA_0} - \varphi_{PA}\right)\right]. \tag{7}$$

By integrating the theories of magnetic torsional viscous phase relaxation and polarized PA phase extraction, this work directly correlates the phase relaxation to viscosity, establishing it as a direct proxy for this physical quantity. This method overcomes the statistical uncertainties inherent in passive microrheology through deep-penetrating active actuation. Positioning drift and boundary effects are eliminated by employing a rotational driving scheme. Furthermore, it overcomes the statistical uncertainty of the traditional single-frequency threshold determination method and enables dynamic and high-precision monitoring of viscosity phase relaxation [39,40].

3. RESULTS

A. Theoretical Simulation

To establish a robust foundation for MTPAV based on magnetically driven phase relaxation, we first validated the core physical model through numerical simulation. Figure 2(a) depicts the angular displacement of a model magnetic rotor (aspect ratio $L/D = 4$) driven by a rotating magnetic field ($B = 0.28$ T, $f = 0.4$ Hz) in media of varying viscosity. A clear transition from synchronous rotation to asynchronous motion is observed as viscosity increases. This manifests as a growing $\Delta\varphi$ between rotor orientation and the driving field, a consequence of the viscous drag torque overcoming the magnetic driving torque. This simulation visually confirms the genesis of viscosity-dependent phase relaxation, which forms the cornerstone of measurement principle. It is inferred in the deterministic relationship between fluid viscosity (η) and the induced phase relaxation of a magnetic rotor, as derived from the balance of magnetic and viscous torques. The result at the short times illustrates the acceleration phase of the rotor from standstill to synchronous rotation, which can be effectively bypassed by employing a pre-rotation step in the experimental design (see Supplement 1 for the initial rotational dynamics). A systematic parametric sensitivity analysis is performed to evaluate the influence of key experimental variables on the quantified viscosity output. Under reference conditions ($B = 0.28$ T, $L/D = 4$, $M = 20$ A/m, $f = 0.5$ Hz), the influence of these four parameters on quantitative viscosity measurement was investigated using the control-of-variables method [Figs. 2(b)–2(e)]. The magnetic field strength showed a modest influence, causing only a minor variation in the maximum detectable viscosity [Fig. 2(b)]. In contrast, the rotor aspect ratio L/D exhibited a pronounced nonlinear effect [Fig. 2(c)]. As L/D increased from 3 to 7, The max η decreased substantially from 0.12 to 0.04 Pa · s. This trend highlights that rotors with a lower L/D offer higher measurement sensitivity. The magnetization M of the rotor demonstrated a direct linear proportionality with the max η [Fig. 2(d)], underscoring the importance of selecting the rotor's magnetic moment for consistent performance. Across a range of driving frequencies (0.5−2 Hz), a linear relationship exists between the medium viscosity (η) and the sine of the phase relaxation angle ($\sin\Delta\varphi$), conforming to the theoretical model. The relationship holds until $\Delta\varphi$ reaches $\pi/2$, beyond which the magnetic torque reverses, leading to asynchronous rotation and defining the upper limit of measurable viscosity for a given frequency. From these linear correlations, Fig. 2(f) was derived by selecting the viscosity value corresponding to $\sin\Delta\varphi = 1$ as the measurable range at the corresponding driving frequency obtained from Fig. 2(e). This indicated that lower frequencies enable the measurement of higher viscosity fluids (up to ∼0.24 Pa · s), while higher frequencies extend the range for lower viscosity samples.

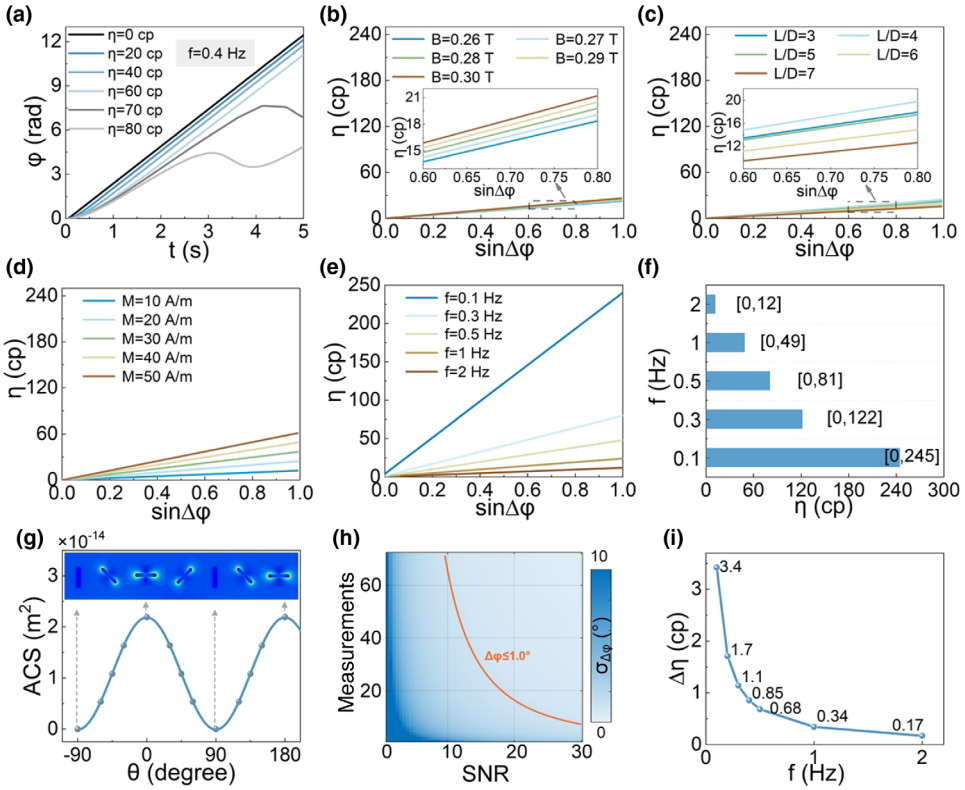

Fig. 2. Modeling validation and parametric analysis of magnetically driven phase relaxation for polarized PA viscometry. (a) Simulated angular displacement of the magnetoplasmonic rotor in media with increasing viscosity. (b–d) Parametric sensitivity analysis quantifying the influence of key system parameters on the maximum measurable viscosity: (b) magnetic field strength B (0.26−0.30 T), (c) rotor aspect ratio L/D (3–7), and (d) rotor magnetization M (10−50 A/m). (e) Quantitative relationship between viscosity and phase relaxation ($\Delta\varphi$) and corresponding curves of viscosity and $\Delta\varphi$ at varying rotational frequencies. (f) Experimentally accessible viscosity measurement ranges derived from the linear fit in (e) for each rotational frequency. (g) Finite-element simulation of the electric-field distribution and absorption cross section of the magnetoplasmonic rotor under polarized-light excitation. (h) Phase detection accuracy heatmap based on CRB analysis. (i) Viscosity measurement uncertainty propagated from the phase estimation error. At a fixed SNR of 15 (phase error = 0.014 rad), the corresponding viscosity uncertainty is plotted against driving frequency.

The feasibility of tracking the rotor's rotational phase via polarized PA detection was verified through finite-element simulation. Figure 2(g) shows the variation in the optical absorption cross-section of the rotor as a function of its orientation relative to a fixed light polarization axis. The simulated $\cos^2\theta$ dependency confirms that the PA signal amplitude effectively encodes the rotor's angular position, enabling the decoding of its rotational phase through polarization-resolved PA measurements. The ultimate precision of this phase-decoding method is governed by fundamental detection limits. We employed Cramér–Rao lower bound (CRB) analysis to quantify the theoretical lower bound for phase estimation error (see Supplement 1 for the related theoretical derivation). Figure 2(h) shows a heatmap of $\Delta\varphi$ as a function of both the number of measurements M and the signal-to-noise ratio (SNR). This analysis illustrats the trade-off between data acquisition time and signal quality required to achieve a desired phase precision. Finally, we translated this fundamental phase precision into the practical metric of viscosity measurement uncertainty [Fig. 2(i)]. For a fixed, experimentally achievable SNR of 15 dB and M of 36, resulting in a phase error of 0.014 rad, the corresponding uncertainty in viscosity was calculated across the 0−2 Hz frequency range. The uncertainty remains remarkably low, reaching only 0.17 cp at 2 Hz. This high precision, stemming from the sensitive phase detection scheme, demonstrates the strong potential of the magnetically driven phase relaxation PA method for accurate viscometry across a broad dynamic range.

B. Experimental Demonstration

To experimentally realize the MTPAV, we designed and synthesized a multifunctional magnetic-plasmonic nanorotor that integrates magnetic responsivity for driven rotation with a strong, polarization-dependent PA signal for optical readout. The synthesis route, illustrated in Fig. 3(a), involves several key steps [41,42]. Non-magnetic FeOOH nanorods were first coated with a SiO_2 layer via the Stöber method to preserve their anisotropic morphology and prevent magnetic aggregation. Subsequent high-temperature reduction in diethylene glycol converted the core to magnetic Fe_3O_4, followed by surface functionalization with thiol groups. Finally, pre-synthesized Au nanorods were grafted onto the magnetic core via Au-S bonds to form the final parallel-linked heterostructure, optimizing optical absorption and magnetic coupling. The preparation method and part of characterization of nanorotors are provided in Supplement 1. The physicochemical properties critical for viscometry were thoroughly characterized. Transmission electron microscopy (TEM) confirmed the parallel-linked rod-like morphology [insets, Fig. 3(b)], with a measured aspect ratio of approximately 4, aligning with the simulation-optimized geometry. Dynamic light scattering revealed

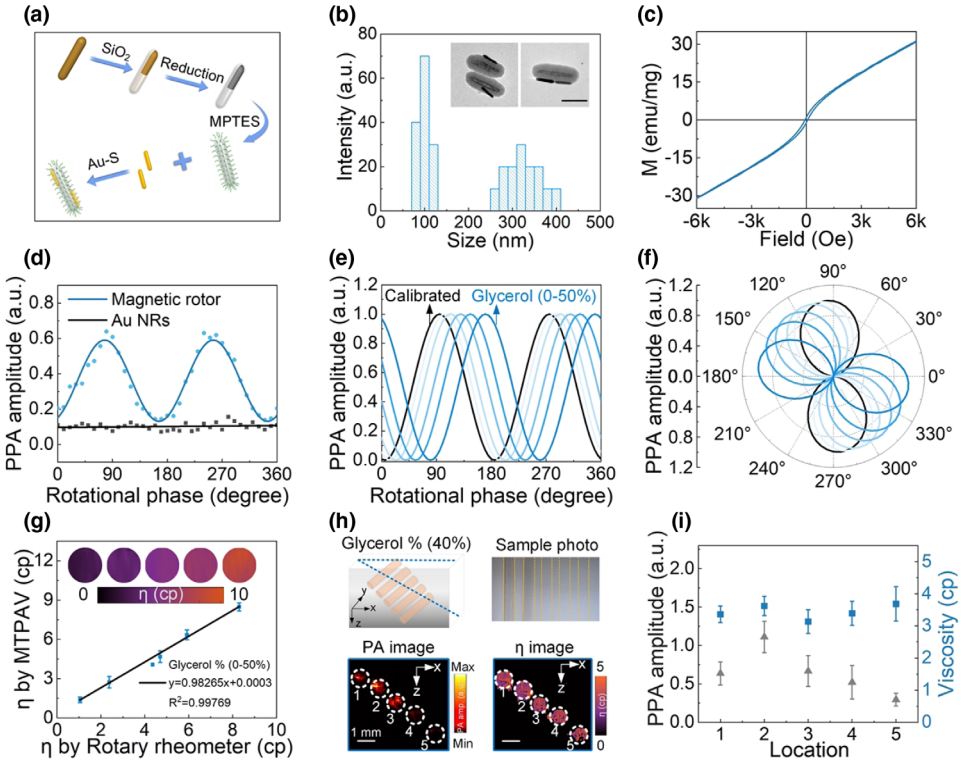

Fig. 3. Characterization of magnetic-plasmonic nanorotors and experimental validation of phase-relaxation PA viscometry in various liquid environments. (a) Schematic illustration of the synthesis process for the magnetic-plasmonic nanorotors. (b) Hydrodynamic size distribution of the synthesized nanorotors. Insets show representative TEM images. Scale bar: 200 nm. (c) Magnetic hysteresis loop of the nanorotors. (d) Polarization-resolved PA signal amplitude as a function of the rotational phase for non-magnetic Au nanorods (control) and the magnetic-plasmonic nanorotors under a rotating magnetic field. (e) PA signal amplitude curves (blue) during magnetically driven rotation of the nanorotors dispersed in glycerol–water mixtures with increasing viscosities (0%, 20%, 30%, 40%, and 50% v/v glycerol). The corresponding calibration curves (black) relate the phase relaxation ($\Delta\varphi$) to the rotational phase. (f) Polar coordinate representation of the data in (e), clearly illustrating the amplitude-encoded rotational phase and the progressive phase shift with increasing viscosity. (g) Linear regression between viscosities quantified by the phase-relaxation PA method and the reference values measured by a rotational rheometer, showing excellent agreement ($R^2 = 0.9977$). (h) Schematic diagram of viscosity samples positioned at different axial depths and photograph of the actual experimental sample arrangement at the top. B-scan PA amplitude images (left) and the corresponding reconstructed viscosity maps (right) of identical viscosity samples (40% glycerol–water) embedded at different depths within a tissue-mimicking phantom. Scale bar: 1 mm. (i) Statistical analysis of the data in (h).

a monodisperse hydrodynamic size distribution centered around ~300 nm [Fig. 3(b)]. The magnetic hysteresis loop [Fig. 3(c)] showed a magnetization of about 20 emu/mg, providing sufficient magnetic moment for controlled rotation under moderate field strengths. Furthermore, numerical simulations and experimental proofs, which confirm that the thermal effects of the nanorotor do not adversely affect the measurement method (see Supplement 1).

The core function of the nanorotor, encoding its rotational phase into the PA signal, was verified experimentally (see Supplement 1 for the detailed composition of the MVPAV system). The lateral resolution of the imaging system is 7.8 μm. Under a 2 Hz rotating magnetic field, the PA amplitude from the magnetic-plasmonic nanorotors exhibited a distinct $\cos^2\theta$ modulation as a function of rotational phase [Fig. 3(d), blue curve], in stark contrast to the phase-independent signal from non-magnetic Au nanorods [Fig. 3(d), gray curve]. This confirmed the successful polarization-resolved readout of the rotor's rotational phase. We then quantified viscosity by measuring the $\Delta\varphi$ induced by viscous drag. The nanorotors were dispersed in glycerol–water mixtures of known viscosity (0−50%v/v glycerol). As shown in Figs. 3(e) and 3(f), the acquired PA amplitude curves (blue) systematically shifted along the phase axis as viscosity increased. This shift represents the growing $\Delta\varphi$ between the rotor's orientation and the driving magnetic field, extracting the phase relaxation for each sample combining with the corresponding calibration curves [Fig. 3(e), gray curve]. A plot of the PA-derived viscosity against reference values from a rotational rheometer [Fig. 3(g)] yielded an excellent linear correlation ($R^2 = 0.9977$), validating the accuracy of the method across a physiologically relevant viscosity range. A key advantage of PA-based detection is its potential for depth-resolved measurements. To demonstrate this, we embedded identical viscosity samples (40% glycerol–water mixture containing nanorotors) at varying depths within a tissue-mimicking phantom (agar, 3%). The B-scan PA amplitude images [Fig. 3(h), left] show the expected decrease in signal intensity with depth due to optical attenuation. Crucially, however, the viscosity maps reconstructed from the phase-relaxation analysis [Fig. 3(h), right] displayed a uniform viscosity value regardless of depth. This is quantitatively supported by the statistical analysis in Fig. 3(i), which shows that while the raw PA amplitude decays exponentially with depth, the computed viscosity remains constant within a narrow error margin. The assessment of viscosity measurement shows that it is robust in terms of changes in probe concentration,

as shown in Supplement 1. These results collectively demonstrate that despite depth-dependent SNR degradation, phase extraction remains unbiased, and the associated viscosity uncertainty is shown to be negligible for practical imaging depths.

C. Biological Applications

To demonstrate the effectiveness of the MTPAV in biological systems, we first quantitatively measured the viscosity of fresh blood samples obtained from an adult New Zealand rabbit, including anticoagulated whole blood, as well as serum and plasma samples after centrifugation [Fig. 4(a)]. The real-time PA amplitude signals of nanorotors during rotation were shown in Fig. 4(b). The corresponding whole blood sample with higher viscosity exhibited a greater rotational phase relaxation. Quantitative calculation using Eq. (7) yielded the viscosity measurements of the blood samples, with serum, plasma, and whole blood viscosities determined as 1.31, 3.15, and 7.89 cp, respectively. The comparison with rotational rheometry results showed an R^2 value exceeding 0.95. These results indicate that the proposed method can achieve accurate quantitative viscosity measurements in low-viscosity physiological environments such as blood. To validate the dynamic viscosity measurement capability of this method, real-time monitoring of dynamic viscosity changes during blood coagulation was designed and performed in Fig. 4(d). The dynamic range of the presented method should be stated as from 0.5 to 10 s. When the driving frequency is 2 Hz, the time resolution of viscosity measurement by the proposed method is at the sub-second level. Centrifuged plasma samples were recalcified to initiate coagulation, and viscosity evolution was recorded over 10 min. A consistent trend in viscosity change was observed compared to rotational rheometer measurements, showing a nonlinear increase in viscosity that plateaued after approximately 6 min, indicating completion of the phase transition. Notably, unlike rotational rheometers, whose single-spindle geometry introduces systematic overestimation at low viscosities owing to fluid inertia and limited torque sensitivity, the MTPAV provides more reliable measurements during continuous changeable processes [Fig. 4(d)]. The PA amplitude extracted during the initial and plateau coagulation phases are shown in Fig. 4(e), where the phase relaxation angle at 8 min is significantly larger than that at 3 min. This contrast clearly demonstrates the feasibility of dynamic viscosity tracking using the method throughout the coagulation process. Subsequently, the Y-type microfluidic device was placed on the surface and a depth of 2.4 mm of the chicken breast. Before and after adding the coagulant $CaCl_2$, MTPAV was performed at different depths to verify the deep tissue viscosity imaging capability of this method [Figs. 4(f)–4(h)]. The results show that the viscosity at a depth of

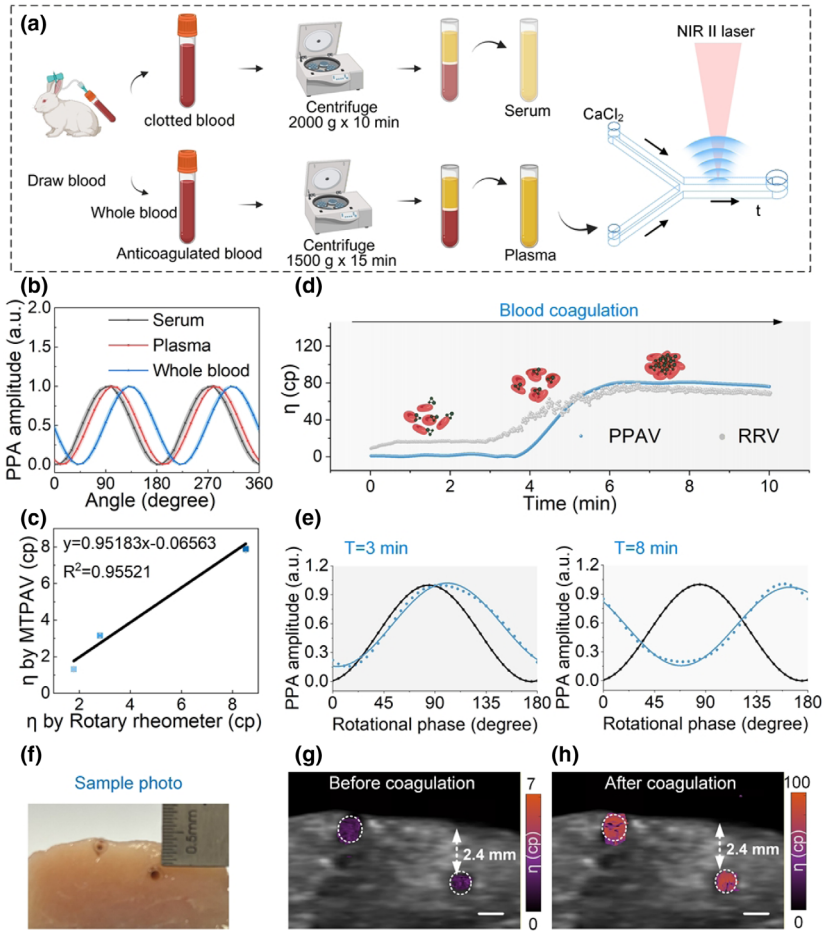

Fig. 4. Blood viscosity analysis. (a) Schematic diagram. (b) Viscosity measurements of adult New Zealand rabbit blood samples (serum, plasma, and whole blood). (c) linear correlation analysis with rotational rheometer measurements. (d) Temporal evolution of viscosity during blood coagulation measured by phase-relaxation PA viscometry (blue) compared with conventional rheological testing (gray). (e) PA amplitude phase-relaxation curves at 3 and 8 min after the onset of coagulation. (f) A cross-sectional view of the sample inserted into the surface and a depth of 2.4 mm of the chicken breast. (g), (h) The viscosity cross-sectional images before and after solidification, respectively. Scale bar: 1 mm.

2.4 mm within the *in vitro* biological tissue can now be quantitatively measured. This is the maximum depth of the tissue for which quantitative measurement of local viscosity has been conducted so far. The method's robustness against depth-dependent signal attenuation underscores its suitability for probing viscosity in complex, scattering environments such as biological tissues. These results demonstrate the ability of the method to perform dynamic viscosity measurements with high accuracy and spatial resolution in the process of blood coagulation.

The proposed methodology was further extended to living biological systems to assess its capability in mapping complex spatiotemporal viscosity dynamics. Given that morphogenesis during development is accompanied by changes in mechanical signals, the dynamic viscosity of embryonic tissues during early developmental stages was examined, elucidating spatiotemporal changes in the viscous properties of the developing morphology [43,44]. As illustrated in Fig. 5(a), early zebrafish embryogenesis exhibits a spatially heterogeneous viscosity pattern. The phase relaxation between the center and the margin of wild-type zebrafish blastoderm was dynamically monitored at 2 and 4.3 h post-fertilization (hpf) using PA viscometry. The results revealed an abrupt ∼5.24-fold decrease in the central region at 2 hpf [Fig. 5(b)] compared to 4.3 hpf [Fig. 5(c)], whereas the phase delay in the marginal zone remained largely consistent, confirming tissue fluidization—a phenomenon key to morphogenesis. This work further achieved the first spatiotemporal 3D viscosity gradient mapping during zebrafish development, revealing significant heterogeneity between marginal and central zones during the protoganglionic stage [Figs. 5(d) and 5(e)]. At 2 hpf, the blastoderm exhibited uniform viscosity, which may be attributable to its composition of highly adhesive cells with extensive intercellular contacts and minimal mesenchymal gaps. At the onset of the dome stage in zebrafish embryos, the viscosity of the deep cell tissue in the central region of the blastoderm decreases sharply by approximately sixfold, while the viscosity in the marginal region remains unchanged. This is due to mitotic cell rounding in the central blastoderm, which disrupts intercellular connections, allowing cells to slide past each other more easily and leading to a reduction in viscosity. In contrast, the marginal region enhances cortical actomyosin contractility, which stabilizes E-cadherin at cell–cell junctions, thereby resisting the disruptive effects of cell division and maintaining a high-viscosity state. With continued development, the central viscosity gradually increased, likely driven by subsequent cell proliferation. These results demonstrate that the proposed method enables precise and dynamic imaging of this critical physicochemical process. Such spatiotemporally regulated viscosity ensures that embryonic deformation occurs at the right location (center) and the right time (onset of doming), thereby facilitating the proper execution of developmental programming.

4. DISCUSSION AND CONCLUSION

This study introduces a novel approach for quantitatively mapping spatiotemporal variations in viscosity during in-body rotational microrheology. The methodology combines theoretical modeling, numerical simulations, and experimental measurements to establish an analytical relationship between viscosity and rotational phase relaxation angle. Additionally, a new technique utilizing polarized PA decoding of rotational vectors is proposed to track dynamic phase relaxation angles. The findings, which align well with results from macroscopic rheological tests, enable real-time visualization of dynamic viscosity changes during coagulation. Notably, we present, for the first time, spatiotemporal viscosity mapping during early zebrafish morphogenesis, underscoring the method's efficacy in capturing viscosity dynamics in intricate biological settings.

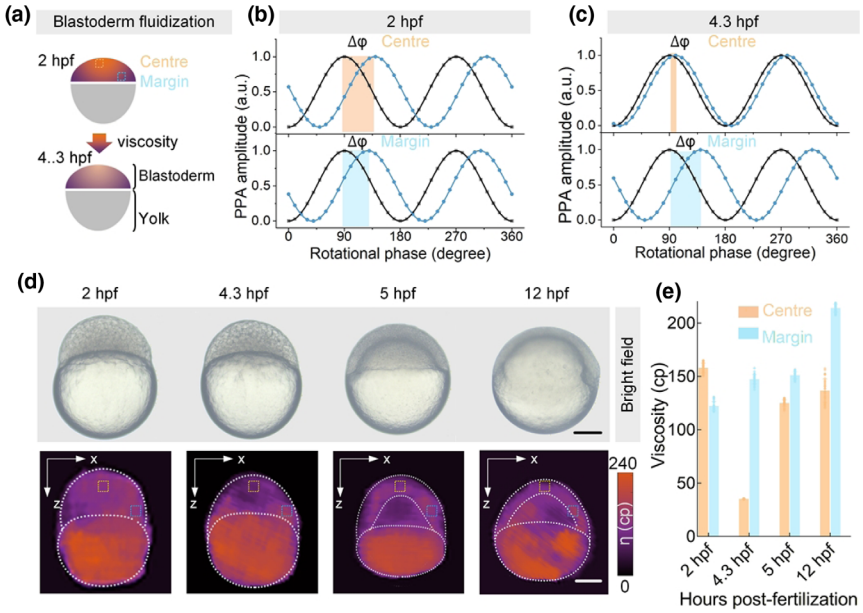

Fig. 5. Spatiotemporal mapping of viscosity dynamics in the zebrafish blastoderm during early development. (a) Schematic illustration of blastoderm fluidization, showing that the central blastocoel undergoes a transient viscosity decrease before the blastoderm-dome stage, followed by gradual recovery. (b), (c) Dynamic tracking of phase-relaxation angles at the central and marginal blastoderm regions at 2 h post-fertilization (hpf) and 4.3 hpf. (d) Bright-field micrographs of wild-type zebrafish embryos at 2, 4.3, 5, and 12 hpf, overlaid with viscosity distribution maps reflecting developmental progression. Scale bar: 0.2 mm. (e) Statistical comparison of viscosity between central and peripheral blastoderm regions at corresponding stages.

It should be noticed that depolarization induced by biological tissues represents an important factor affecting polarization-sensitive phase decoding. In the present study, the FFT-based phase extraction approach reduces the influence of depolarization-induced signal amplitude attenuation by retrieving phase information independent of absolute intensity, enabling robust viscosity quantification in highly scattering tissues. Future studies may explore polarization-sensitive wavefront shaping combined with PA feedback to characterize and compensate tissue-induced polarization distortions, thereby further improving phase decoding accuracy. The phase relaxation angle measured at a single driving frequency represents a composite response of the medium's complex modulus. Accordingly, the viscosity values reported herein should be interpreted as the dynamic viscosity $\eta' = G''/\omega$ at the specific frequency applied. This parameter adequately captures the mechanical heterogeneity dominated by viscous dissipation in biological processes such as blood coagulation and embryonic development. The frequency-dependent behavior of φ enables full viscoelastic characterization. The synchronous low-frequency phase delay predominantly reflects viscous dissipation for equivalent viscosity extraction, whereas the asynchronous oscillation amplitude and frequency response capture the elastic recovery information. Recording the full frequency spectrum in future studies will decouple these components, achieving complete rheological characterization of complex media. At the same time, we acknowledge the inherent limitations of the approach, including the rotor size dictates the spatiotemporal resolution of the measurement and the apparent viscosity obtained in structured fluids reflects the mechanical heterogeneity at specific length scales. Multiscale rotor design provides an effective method for the study of mechanical parameters across different scales.

5. MATERIALS AND METHODS

A. Experimental Setup

A 1064 nm pulsed laser (DS20HE-1064D/R, PHOTONICS) with a repetition rate of 1 kHz was used as the excitation source. The laser was first converted into linearly polarized light using a half-wave plate and a polarizing beam splitter. The output polarization direction was kept fixed. The magnetic field was generated by a custom-designed Halbach array with a hollow diameter of 10 mm. The central magnetic flux density was 0.2 T, and the uniform magnetic-field region was approximately 5 mm around the center. while the magnetic field was rotated to modulate the orientation of the anisotropic magnetic nanorotors and thus the polarization-dependent PA signal. The laser beam was focused onto the sample through an objective lens with NA = 0.25. PA signals were detected using a hollow focused ultrasound transducer with a central frequency of 10 MHz, a bandwidth of 95%, and a focusing radius of 15.3 mm. The detected signals were filtered using a BLP-21.4+ filter (Mini-Circuits), amplified by an LNA-650 amplifier (RF Bay Inc.), and then acquired by a high-speed digitizer (M2p 5960 ×4, Spectrum). The sample was mounted on a two-dimensional motorized scanning stage driven by high-precision stepper motors (LNR502/M, Thorlabs) with a 1 μm positioning step size.

B. Numerical Analysis

Solve the torque balance differential equation Formula (1), according to the experimentally measured geometric size of the rotor and the parameters of the magnetic field setting, where the initial values are set to $L/D = 4$, $B = 0.28$ T, $M = 20$ A/m, the rotation frequency is set to 0.4 Hz. The angular displacement curves under different viscosity gradients are calculated, respectively. By defining that the maximum angle between the magnetic moment direction of the magnetic rotor and the magnetic field direction is 90°, Because more than 90° will result in reduced angular displacement of the rod rotation due to the reverse torque imparted by the magnetic field, asynchronous response will occur. Therefore, by defining the critical relaxation angle, the measurement range of viscosity at different rotational frequencies can be calculated.

C. System Calibration

The purpose of the zero-relaxation calibration is to define the instantaneous rotational phase of the external magnetic field without any viscosity-induced phase relaxation. A polarization-sensitive standard sample was prepared with its absorption principal axis predefined and fixed. The absorption axis of this standard sample was then aligned with the direction of the external magnetic field, and mechanically fixed. During calibration, the standard sample was rotated synchronously with the magnetic-field, and the corresponding polarization-modulated PA signal was recorded. Because the standard sample is rigidly fixed and does not experience viscous rotational relaxation, the phase of the obtained modulation signal directly represents the rotational phase of the external magnetic field, defined as the zero-relaxation reference phase. For each experiment, the magnetic-field controller was initialized to the same predefined starting azimuth. The initial magnetic-field phase was reset to this home position before the next measurement was started. Under this condition, additional recalibration is not required between consecutive experiments. Recalibration is only necessary when the direction of the optical excitation, magnetic-field direction, or detection module is changed.

D. Data Processing

Before extracting the phase-relaxation angle, the dynamic state of the nanorotors was assessed by Fourier analysis of the PA time-domain signals. The response was operationally classified as synchronous when the dominant PA modulation frequency coincided with the magnetic driving frequency. Only measurements within this frequency-synchronized regime were used for steady-state phase-delay extraction and quantitative viscosity inversion. Data showing a deviation of the dominant response frequency from the driving frequency, spectral broadening associated with unstable rotation, or other signatures of step-out behavior were excluded from the present phase–viscosity inversion.

E. Glycerol–Water Experimental Setup

Various glycerol–water solutions were prepared with different concentrations (0%, 20%, 30%, 40%, and 50%) by mixing glycerol and water. Subsequently, magnetic nanorotor suspension (100 μL, 1 mg/mL) was added to each solution and thoroughly mixed to achieve a uniform dispersion of nanorods in the solution. The solutions were then placed in a 3D printed acrylic circular

array of holes, sealed with a polyethylene film to prevent the formation of bubbles. The entire experiment was conducted at room temperature, with the frequency of the rotating magnetic field set at $f = 2$ Hz to ensure that the measured viscosity fell within the desired range. The mapping of various viscosity gradients was performed by scanning the xy plane using a motor drive.

F. Zebrafish Embryo Collection and Microinjection

Wild-type (AB strain) zebrafish was maintained in a circulating water system at a temperature of 28.5°C under a 14 h light/10 h dark photocycle. Embryos were obtained through natural mating and subsequently cultured in standard embryo culture medium (E3 solution). Within one-hour post-fertilization, a precise microinjection system comprising pneumatic injectors and micromanipulators was utilized. A magnetic rotor suspension (7 nL, 1 mg/mL) was then injected into the yolk region of the embryos. Subsequently, the injected embryos were expeditiously transferred to fresh E3 medium and placed in a constant temperature incubator at 28.5°C until the designated developmental time point for assessment.

G. Hemorheology

Healthy adult New Zealand rabbits were utilized for this study. Blood samples were drawn using syringes with appropriate anticoagulants. Whole blood was collected in ethylenediaminetetraacetic acid (EDTA) anticoagulant tubes, while samples for coagulation kinetics studies and plasma samples were collected in sodium citrate tubes at a 1:9 volume ratio to blood. Whole blood viscosity of EDTA-anticoagulated samples was measured at room temperature immediately after collection, and all assessments were completed within an hour of collection. Subsequently, the sodium citrate anticoagulated whole blood was centrifuged at 1500 × g and 25°C for 15 min. The resulting supernatant was aspirated to obtain sodium citrate plasma. Blood samples without anticoagulants were left to coagulate naturally for an hour in a water bath at a constant temperature of 37°C. After coagulation, they were centrifuged at 2000 × g for 15 min to collect the serum supernatant. Prior to testing (whole blood, plasma, and serum), all blood samples were gently mixed with a magnetic rotor (100 μL, 1 mg/mL) at a volume fraction of 0.1%. To prevent blood cell damage, mix by repeatedly inverting. Sodium citrate anticoagulant plasma was utilized for coagulation kinetics assessments. Before testing, plasma samples and a preheated 0.1 M calcium chloride ($CaCl_2$) solution were each placed in a specific microfluidic mold and combined through simultaneous syringe manipulation to reverse anticoagulation and initiate coagulation anew. The introduction and mixing of $CaCl_2$ were noted as the initial moment for dynamic monitoring.

H. Spatiotemporally Resolved Viscosity Imaging

The same embryo is placed in a custom dish filled with low-melting agarose and is gently embedded for fixation after adjusting the embryo posture under a microscope. The embryo's position is delicately adjusted under a microscope before fixation. Pre-scanning using PA microscopy delineates the central and marginal regions of germ layer cells to ascertain embryo structure and target positioning. Dynamic viscosity data at these regions are acquired by measuring viscosity changes at different developmental stages (2 hpf and 4.3 hpf) using a rotating magnetic field frequency of 0.1 Hz. To assess the spatial viscosity profile of embryos at various developmental stages (2, 4.3, 5, and 12 hpf), embryos undergo developmental retardation with low doses of anesthetic. Cross-sectional B-scan profiles are generated through point measurements of line scans.

I. Rotational Rheometer

The volumetric rheological viscosity of glycerol–water solution and blood measured by the rotational rheometer used in this paper were all measured by HAAKE MARS III. Among them, when the ratio of glycerol to water is 0 (pure water) and 20%, and the ultra-low viscosity samples of plasma and serum samples are measured, the double-gap cylinder rotor test is used, while 30%, 40%. Viscosity measurements of 50% glycerin–water mixtures with whole blood samples and plasma during coagulation were performed using coaxial cylinders.

Funding. National Key R&D Program of China (2024YFF0507203, 2024YFF0507201); National Natural Science Foundation of China (62575104, 62335007, 12304483); Guangdong Basic and Applied Basic Research Foundation (2026A1515010458, 2024A1515010287, 2024A1515010522); China Postdoctoral Science Foundation (2024M750971); Open Fund of the State Key Laboratory of Integrated Optoelectronics (IOSKL2025KF10); Youth S&T Talent Support Program of Guangdong Provincial Association for Science and Technology (SKXRC2025013).

Disclosures. The authors declare no conflicts of interest.

Data availability. All data are available in the main text or supplementary materials. Information requests should be directed at the corresponding authors.

Supplemental document. See Supplement 1 for supporting content.

REFERENCES

1. S. Kamdar, S. Shin, P. Leishangthem, *et al.*, "The colloidal nature of complex fluids enhances bacterial motility," Nature **603**, 819–823 (2022).
2. Y. Chen, J.-H. Huang, C. Phong, *et al.*, "Viscosity-dependent control of protein synthesis and degradation," Nat. Commun. **15**, 2149 (2024).
3. K. Trachenko, "Constraints on fundamental physical constants from biofriendly viscosity and diffusion," Sci. Adv. **9**, eadh9024 (2023).
4. V. Sandoghdar, "Essay: exploring the physics of basic medical research," Phys. Rev. Lett. **132**, 090001 (2024).
5. C. Datt and G. J. Elfring, "Active particles in viscosity gradients," Phys. Rev. Lett. **123**, 158006 (2019).
6. T. Markovich and T. C. Lubensky, "Odd viscosity in active matter: microscopic origin and 3D effects," Phys. Rev. Lett. **127**, 048001 (2021).
7. K. Shoele and P. S. Eastham, "Effects of nonuniform viscosity on ciliary locomotion," Phys. Rev. Fluids **3**, 043101 (2018).
8. V. A. Shaik and G. J. Elfring, "Hydrodynamics of active particles in viscosity gradients," Phys. Rev. Fluids **6**, 103103 (2021).
9. C. Huerta-López, A. Clemente-Manteca, D. Velázquez-Carreras, *et al.*, "Cell response to extracellular matrix viscous energy dissipation outweighs high-rigidity sensing," Sci. Adv. **10**, eadf9758 (2024).
10. A. Sharma, R. Thakur, S. Jose, *et al.*, "Viscosity variation in fluid flows across scale," arXiv (2025).
11. J. A. Lawrence and P. S. Steeg, "Mechanisms of tumor invasion and metastasis," World J. Urol. **14**, 124–130 (1996).
12. J. P. Baskaran, A. Weldy, J. Guarin, *et al.*, "Cell shape, and not 2D migration, predicts extracellular matrix-driven 3D cell invasion in breast cancer," APL Bopeng. **4**, 026105 (2020).
13. A. Mongera, P. Rowghanian, H. J. Gustafson, *et al.*, "A fluid-to-solid jamming transition underlies vertebrate body axis elongation," Nature **561**, 401–405 (2018).
14. N. I. Petridou, B. Corominas-Murtra, C.-P. Heisenberg, *et al.*, "Rigidity percolation uncovers a structural basis for embryonic tissue phase transitions," Cell **184**, 1914–1928.e19 (2021).
15. K. Bera, A. Kiepas, I. Godet, *et al.*, "Extracellular fluid viscosity enhances cell migration and cancer dissemination," Nature **611**, 365–373 (2022).

16. M. Dessard, J.-B. Manneville, and J.-F. Berret, "Cytoplasmic viscosity is a potential biomarker for metastatic breast cancer cells," Nanoscale Adv. **6**, 1727–1738 (2024).
17. N. Kasireddy, E. M. Cummins, H. Q. Pham, *et al.*, "Small-volume noncontact assessment of blood coagulation via acoustic tweezing coagulometry," Blood **138**, 3178 (2021).
18. J. Kang, J. S. Oh, B. J. Kim, *et al.*, "High blood viscosity in acute ischemic stroke," Front. Neurol. **14**, 1320773 (2023).
19. P.-H. Wu, D. R.-B. Aroush, A. Asnacios, *et al.*, "A comparison of methods to assess cell mechanical properties," Nat. Methods **15**, 491–498 (2018).
20. W.-S. Kim, S. Min, S. K. Kim, *et al.*, "Magneto-acoustic protein nanostructures for non-invasive imaging of tissue mechanics in vivo," Nat. Mater. **23**, 290–300 (2024).
21. I. Sack, "Magnetic resonance elastography from fundamental soft-tissue mechanics to diagnostic imaging," Nat. Rev. Phys. **5**, 25–42 (2022).
22. W. Jia, S. Xia, X. Jia, *et al.*, "Ultrasound viscosity imaging in breast lesions: a multicenter prospective study," Acad. Radiol. **31**, 3499–3510 (2024).
23. T. Meyer, J. Castelein, J. Schattenfroh, *et al.*, "Magnetic resonance elastography in a nutshell: tomographic imaging of soft tissue viscoelasticity for detecting and staging disease with a focus on inflammation," Prog. Nucl. Magn. Reson. Spectrosc. **144–145**, 1–14 (2024).
24. F. Alshomrani, "Recent advances in magnetic resonance imaging for the diagnosis of liver cancer: a comprehensive review," Diagnostics **15**, 2016 (2025).
25. F. L. Durhuus, M. Beleggia, and C. Frandsen, "Magnetic and viscous dynamics of spheroidal nanoparticles," Phys. Rev. B **110**, 144425 (2024).
26. J. Shang, Y. Ma, X. Liu, *et al.*, "Single–particle rotational microrheology enables pathological staging of macrophage foaming and antiatherosclerotic studies," Proc. Natl. Acad. Sci. U.S.A. **121**, e2403740121 (2024).
27. H.-H. Jeong, A. G. Mark, T.-C. Lee, *et al.*, "Active nanorheology with plasmonics," Nano Lett. **16**, 4887–4894 (2016).
28. G. R. Heath, E. Kots, J. L. Robertson, *et al.*, "Localization atomic force microscopy," Nature **594**, 385–390 (2021).
29. I. Remer, R. Shaashoua, N. Shemesh, *et al.*, "High-sensitivity and high-specificity biomechanical imaging by stimulated Brillouin scattering microscopy," Nat. Methods **17**, 913–916 (2020).
30. Z. Hajjarian and S. K. Nadkarni, "Technological perspectives on laser speckle micro-rheology for cancer mechanobiology research," J. Biomed. Opt. **26**, 090601 (2021).
31. F. Yang, Z. Chen, P. Wang, *et al.*, "Phase-domain photoacoustic mechanical imaging for quantitative elastography and viscography," IEEE Trans. Biomed. Eng. **71**, 2330–2340 (2024).
32. N. Leartprapun, Z. Zeng, Z. Hajjarian, *et al.*, "Laser speckle rheological microscopy reveals wideband viscoelastic spectra of biological tissues," Sci. Adv. **10**, eadl1586 (2024).
33. F. Català-Castro, S. Ortiz-Vásquez, C. Martínez-Fernández, *et al.*, "Measuring age-dependent viscoelasticity of organelles, cells and organisms with time-shared optical tweezer microrheology," Nat. Nanotechnol. **20**, 411–420 (2025).
34. W. Philippoff, "Angular relationship in rheology," Trans. Soc. Rheol. **12**, 85–102 (1968).
35. D. Lisjak and A. Mertelj, "Anisotropic magnetic nanoparticles: a review of their properties, syntheses and potential applications," Prog. Mater. Sci. **95**, 286–328 (2018).
36. J.-F. Berret, "Local viscoelasticity of living cells measured by rotational magnetic spectroscopy," Nat. Commun. **7**, 10134 (2016).
37. X. Su, Z. Zhang, Y. Wang, *et al.*, "Optical attenuation-resistant photoacoustic tomography with isotropic contrast via polarization-demodulated magnetic orientation awareness," Laser Photonics Rev. **19**, e00916 (2025).
38. Z. Zhang, Y. Shi, L. Xiang, *et al.*, "Polarized photoacoustic microscopy for vectorial-absorption-based anisotropy detection," Opt. Lett. **43**, 5267 (2018).
39. A. Tokarev, I. Luzinov, J. R. Owens, *et al.*, "Magnetic rotational spectroscopy with nanorods to probe time-dependent rheology of microdroplets," Langmuir **28**, 10064–10071 (2012).
40. M. L. Watson, D. L. Brown, A. B. Stilgoe, *et al.*, "Rotational optical tweezers for active microrheometry within living cells," Optica **9**, 1066–1072 (2022).
41. M. Wang, C. Gao, L. He, *et al.*, "Magnetic tuning of plasmonic excitation of gold nanorods," J. Am. Chem. Soc. **135**, 15302–15305 (2013).
42. Z. Li, J. Jin, F. Yang, *et al.*, "Coupling magnetic and plasmonic anisotropy in hybrid nanorods for mechanochromic responses," Nat. Commun. **11**, 2883 (2020).
43. N. I. Petridou, S. Grigolon, G. Salbreux, *et al.*, "Fluidization-mediated tissue spreading by mitotic cell rounding and non-canonical Wnt signalling," Nat. Cell Biol. **21**, 169–178 (2019).
44. X. Liang, Y. Ding, Z. Yuan, *et al.*, "Mechanics of soft-body rolling motion without external torque," Phys. Rev. Lett. **134**, 198401 (2025).